An approach to develop set-on-demand 3D printable limestone-calcined clay-based cementitious materials using calcium nitrate

Chen, Yu; Rahmani, Hossein; Schlangen, Erik; Çopuroğlu, Oğuzhan

Important note
To cite this publication, please use the final published version (if applicable).
Please check the document version above.

An approach to develop set-on-demand 3D printable limestone-calcined clay-based cementitious materials using calcium nitrate

Yu Chen [*], Hossein Rahmani, Erik Schlangen, Oğuzhan Çopuroğlu

Microlab, Faculty of Civil Engineering and Geosciences, Delft University of Technology, Delft, the Netherlands

ARTICLE INFO

ABSTRACT

The implementation of extrusion-based 3D concrete printing (3DCP) in large-scale constructions is currently limited by concerns regarding rheology control and the sustainability of this process. To address these issues, this study presents an approach to develop limestone-calcined clay-based cementitious (LC3) materials accelerated by $Ca(NO_3)_2$ solution in an inline static mixer-based 3DCP setup. Using this approach, a printable mixture containing only about 275 kg/m^3 of Portland cement was formulated that can exhibit a good buildability performance and a 28-day compressive strength of over 30 MPa. Additionally, the effects of adding $Ca(NO_3)_2$ solution on the initial setting time, structural build-up, inline buildability, early-age hydration, and compressive strength of LC3 materials were investigated and discussed. Results show that the addition of $Ca(NO_3)_2$ solution improved the buildability and accelerated initial setting as well as the structuration due to the promoted ettringite precipitation and C–S–H nucleation. Furthermore, compressive strength at 7 and 28 days was improved through increasing the $Ca(NO_3)_2$ dosage, which can be attributed to the formation of NO_3-AFm and the increase in the amount of C–S–H gels.

1. Introduction

Digital fabrication with concrete is proposed as a possible solution in response to the desire to develop a more sustainable built environment [1–4]. Extrusion-based 3D concrete printing (3DCP), also known as the layer-extrusion approach, as one of the most exploited technologies in this context, has received considerable progress over the past years [1,2, 5–7]. However, critical issues related to rheology control and sustainability still hinder the implementation of 3DCP in large-scale construction.

The elimination of formwork in 3DCP process brings great benefits, for instance, reduced construction time, waste, and cost, as well as increased flexibility of architectural design and safety of construction site [8–10], but also imposes stringent requests on the material behavior. Fresh cementitious material should display sufficient fluidity during pumping and must rapidly emerge a high yield stress after layer deposition [11–14]. Earlier studies [15–23] mainly concentrated on developing materials for 1-component (1 K) printing system, which largely depends on thixotropic properties of fresh cementitious materials. However, as pointed out by Refs. [2,16,24], the use of 1 K printing

system appears to be restrained by the relatively short open time and limited structuration rate of thixotropic materials, hindering its application in large-scale construction. To improve the rheology/stiffening control of fresh cementitious materials, 2-component (2 K) printing system is proposed and developed as a more sophisticated method [2, 25–27]. Compared with 1 K printing system, 2 K printing system integrates an additional pre-mixing step, which allows the addition of an activator in the printhead to reach the aim of set-on-demand printing [2]. Therefore, fresh cementitious material with high fluidity and sufficiently long open time can be employed during the pumping process. After inline mixing with activators in the printhead, a final mixture with the desired buildability can be obtained [2,25,27]. Please note that other activation methods that directly or indirectly (using capsules) stimulate the stiffness evolution of fresh cementitious materials, i.e., microwave heating [28–30], ultrasonic pulse [31], and magnetic field [32], can also be applied in this context. Nevertheless, this study only concentrated on the approach of using an activator in the pre-mixing process.

To pre-mix the accelerator, the printhead of 2 K printing system is equipped with a dynamic or static inline mixer [5,33]. By using a dynamic mixer, fast set pastes, e.g., calcium aluminate cement (CAC) paste,

have been successfully used to actively control the rheological and buildability properties of printable cementitious materials [25,34,35]. In contrast, Tao et al. [33] employed a printing setup based on a static inline mixer. In their studies [36,37], limestone-based mortar mixtures containing alkali-free shotcrete accelerator (aluminate-based accelerator) were formulated for inline mixing fresh Portland cement-based mixtures. By using the same setup, Mohan et al. [38] developed similar two-part printable mixtures based on borated calcium sulfoaluminate (CSA) cement and calcium hydroxide. Compared to aluminate-based accelerators and pastes, calcium salts are also a viable option for accelerating the stiffness of 3D printable cementitious materials at relatively low cost but with high efficiency. Unlike aluminate-based accelerators and pastes, which rely primarily on the ettringite precipitation to facilitate structuration, calcium-based salts, i. e., $CaCl_2$ and $Ca(NO_3)_2$, typically stimulate nucleation and dissolution kinetics [2,33,39–41]. Our earlier study [24] attempted to use desalination brine containing high concentrations of calcium chloride ($CaCl_2$) as a source of inorganic accelerators for 3DCP. However, use of $CaCl_2$ is not allowed in steel-rebar reinforced concrete structures due to the early corrosion risk [40], which significantly limits the application of this approach. As an alternative, calcium nitrate ($Ca(NO_3)_2$), which has a slightly lower acceleration efficiency than $CaCl_2$, has been widely used in conventional mold-cast concrete [41]. However, to our knowledge, there has been no research on using $Ca(NO_3)_2$ as an activator in 2 K printing system.

The sustainability of 3DCP is still debated [1], especially regarding the environmental impact of the material selection. The pumping operation of 3DCP limits the use of coarse aggregate and sand content in 3D printable concrete, resulting in a large paste volume and therefore high Portland cement (PC) content in most proposed mixtures [16,35,42]. To reduce the PC content in printable concrete, partial replacement of PC with supplementary cementitious materials (SCMs) seems to be a viable approach [43,44]. Considering their low carbon emissions during the manufacturing process, abundant deposits, and sufficient global supply, calcined clay and limestone stand out as ideal SCMs for developing sustainable concrete in the long term, compared to common SCMs, e.g., blast-furnace slag, fly ash, and silica fume [16,45,46]. Until now, numerous attempts [15,16,47,48] have been made to formulate calcined clay-limestone-based cementitious materials for 3DCP based on the 1 K printing system. However, little attention has been paid to the development of set-on-demand printable materials using this ternary blended system and an inorganic chemical additive, particularly $Ca(NO_3)_2$. Additionally, as reported by Ref. [41], $Ca(NO_3)_2$ not only accelerates alite hydration but also influences aluminate reaction favorably. Furthermore, calcined clays are rich in reactive aluminate phases [45,49], which may interact with NO_3^- to form NO_3-bearing AFm phases [41,50]. Nevertheless, the impact of $Ca(NO_3)_2$ addition on the early-age hydration of limestone-calcined clay-based cementitious materials has so far remained unclear.

To this end, this study aims to introduce an approach to develop limestone-calcined clay-based cementitious materials activated with $Ca(NO_3)_2$ solution in the context of sustainable and set-on-demand 3D printing on the basis of an inline static mixer-based setup. The first part of this paper was to formulate two kinds of pumpable mixtures, including cementitious materials (CM) and acceleration slurries (AS), by using slump flow, flow curve, and pumpability tests. Thereafter, the developed CM and AS with different dosages of $Ca(NO_3)_2$ solution were (inline) mixed to make the final mixture. The effects of adding $Ca(NO_3)_2$ solution on the initial setting time, structural build-up, inline buildability, early-age hydration, and compressive strength of the final mixture were investigated and discussed.

2. Materials and methods

2.1. Set-on-demand printing setup and methodology

Fig. 1 illustrates the set-on-demand printing setup that comprises three components: a Computer Numerical Control (CNC) machine, two progressive-cavity pumps (PFT Swing-M model, Germany), and a customized printhead attached to an inline static mixer. Two material hoses (maximum pressure: 40 bar) with an inner diameter of 25 mm and a length of 5 m are used to connect the customized printhead and pumps. The customized printhead inspired by the twin-pipe system [5] includes a metal pipe with two inlets and a static mixer with 16 mixing baffles. The inner diameter of the pipe is 25 mm. For each baffle, the thickness is about 3 mm, and the length is about 40 mm. Two adjacent baffles have opposite rotational directions. As shown in Fig. 2, there are two stages to developing set-on-demand limestone-calcined clay-based printable cementitious materials. In stage 1, two flowable and pumpable mixtures, i.e., cementitious material and acceleration slurry, can be formulated using a series of methods, including slump flow, flow curve, and inline pumpability tests. Afterward, two composites are inline mixed in the printhead and deposited via the nozzle to form a printed filament/layer, which should show a relatively short initial setting time and desired buildability performance. These behaviors can be assessed by vicat penetration, small amplitude oscillatory shear (SAOS)-time sweep, and inline buildability tests. Detailed experimental procedures were reported in Section 2.3.

2.2. Raw materials and mix designs

The binding materials used in this paper included CEM I 52.5 R Portland cement, calcined clay and limestone powder. Calcined clay containing about 48.8 wt% reactive phases was provided by Argeco, France. The particle size distribution and X-ray diffraction (XRD) pattern of all fines are presented in Fig. 3. It can be found that calcined clay displayed a much coarser grain size than other binding materials, due to the presence of quartz impurity, according to Ref. [16]. In addition, fine quartz sand with 0.125–1 mm particle size was employed as aggregate.

Table 1 presents the mixture compositions of cementitious materials (CM) and acceleration slurries (AS). For CM, the binder mainly comprised Portland cement (55 % of the binder mass) and the blend of calcined clay and limestone powder in a mass ratio of 2:1. The aggregate-to-binder and water-to-binder mass ratios were kept as 1:1 and 0.30. To modify flowability to satisfy the demands for pumping, 0.5–1.0 wt% of polycarboxylate ether-based superplasticizer (SP) were added to CM. A suitable dosage of SP was determined by the assessment of slump flow test (Section 2.3.1). As explained in Refs. [24,36], injecting acceleration solution into the CM directly will significantly decrease the solid-to-liquid ratio of the mixture, weakening the yield stress and buildability. Therefore, the AS containing limestone powder (inert filler) and aggregate were employed as the $Ca(NO_3)_2$ solution carrier. Compared to CM, AS showed similar aggregate-to-binder and water-to-binder (limestone powder is referred to the binding material). For mixtures AS-7 and AS-14, about 7 wt% and 14 wt% (of the limestone powder content) of $Ca(NO_3)_2$ solution were added. To maintain the same liquid volume in different AS mixtures, the water content was adjusted according to the water amount of $Ca(NO_3)_2$ solution. Time zero of CM and AS was selected as the water addition time. Fresh CM, AS, and final mixtures (except for the printability test) were prepared following the mixing protocol in Table 2. For the final mixture, time zero was defined as the start of mixing CM and AS.

2.3. Experimental methods

2.3.1. Slump flow and inline pumpability tests

Hägermann flow table test (Hägermann cone mold: 70 mm in upper internal diameter, 100 mm in bottom inner diameter, and 60 mm in
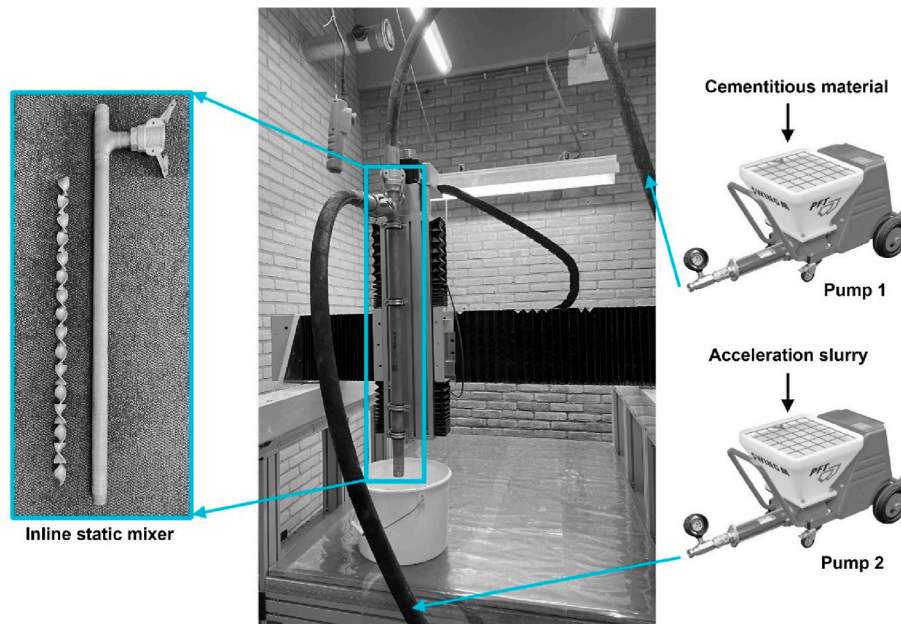
Fig. 1. Set-on-demand 3D concrete printing setup: CNC configuration, progressive-cavity pump (× 2), material hose (× 2), inline static mixer.
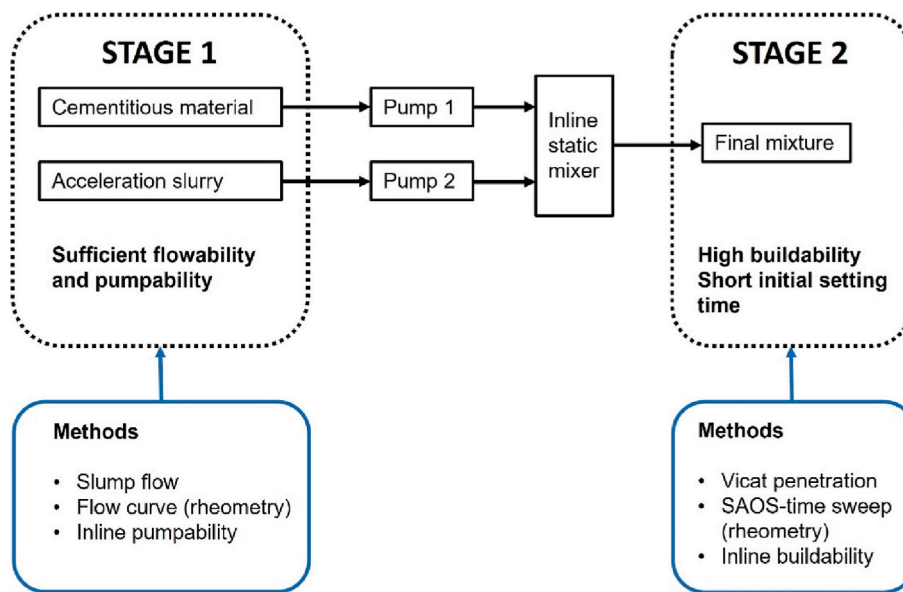
Fig. 2. A roadmap to develop set-on-demand limestone-calcined clay-based printable cementitious materials. Flowable and pumpable cementitious materials and acceleration slurries were formulated in stage 1, and the final mixture that displayed sufficient buildability was developed in stage 2.

height) was employed to determine the flowability of fresh CM and AC mixtures. The test details referred to earlier studies [11,16]. The spread diameter after 25 times of table drops was considered the flowability indicator of the studied mixture. Considering the time required for one printing session (in the lab condition, hopper volume 38 L ÷ material flow rate 0.75–1.5 L/min = 25~51 min), the fresh mixture should maintain proper flowability within the first 1 h of material age. Thus, the slump flow test was conducted at the material age of 10 min, 25 min, 40 min and 60 min.

Inline pumpability test was used to validate whether the developed CM and AS could be used for pumping. This test was performed on a progressive cavity pump (the same as that for printing) with a 2.5 m material hose. About 7 L of fresh mixture was prepared for each test. Different pumping rates (from 20 rpm to 100 rpm with intervals of 20 rpm) were applied and the extruded material was collected for about 10

s at every rate. Therefore, the real-time material flow rate can be computed by the mass of the collected material.

2.3.2. Characterization of rheological behaviors

Rheological behaviors, including flow properties and structural build-up of studied mixtures, were investigated using a rheometer (Anton Paar MCR 302e mode). The flow curve test was employed to determine flow properties of CM and AS. For mortar samples, a measuring stirrer with two hollow blades (diameter: 35.22 mm; height: 25.8 mm) in a building material cell (inner diameter: 70 mm; depth: 100 mm) was employed. In contrast, small amplitude oscillatory shear (SAOS)-time sweep test was applied to paste samples (final mixture) for quantifying the structural build-up. In this case, the setup of a four-blade vane (diameter: 22 mm; height: 40 mm) and a small cylindrical cup (inner diameter: 28.92 mm; depth: 68 mm) was used. In addition, the
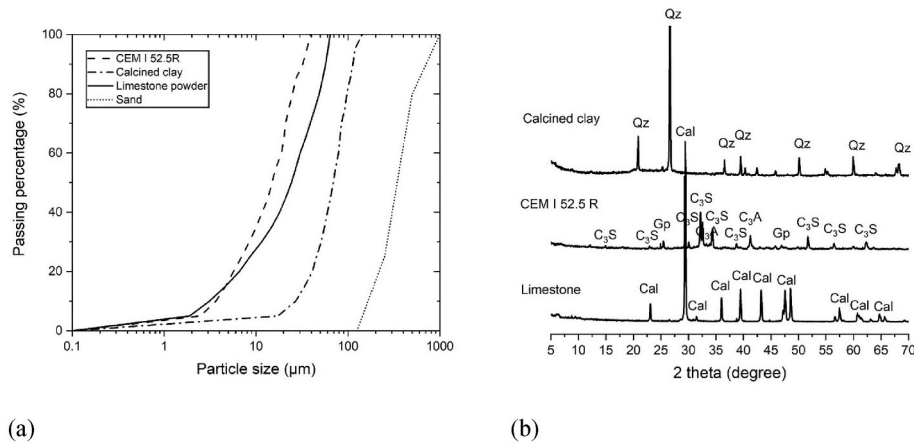
Fig. 3. (A) Particle size distribution of CEM I 52.5 R Portland cement, limestone and calcined clay determined by laser diffractometry. Quartz sand with grain size in the range of 0.125–1 mm; (b) X-ray diffraction patterns (Cu-Kα radiation) of CEM I 52.5 R Portland cement, calcined clay, and limestone powder. Qz - quartz, Gp - gypsum, Cal - calcite.

Table 1
Mix designs of cementitious materials and acceleration slurries.

Cementitious material	Portland cement	Limestone powder	Calcined clay	Water	Aggregate	Superplasticizer (wt.% of the binder)
CM-0.5	0.55	0.15	0.30	0.30	1	0.5
CM-0.6	0.55	0.15	0.30	0.30	1	0.6
CM-0.8	0.55	0.15	0.30	0.30	1	0.8
CM-1	0.55	0.15	0.30	0.30	1	1
Acceleration slurry		Limestone powder		Water	Aggregate	Ca(NO₃)₂ solution* (wt.% of limestone powder in acceleration slurry)
AS-0		1		0.30	1	0
AS-7		1		0.26	1	7
AS-14		1		0.22	1	14

Ca(NO$_3$)$_2$ solution*: 50 wt% of Ca(NO$_3$)$_2$.

Table 2
Mixing protocols for preparing fresh cementitious materials, acceleration slurry and final mixture (for initial setting time and compressive strength tests).

Cementitious material or acceleration slurry	
Time	Procedures
t = 0 min	Slowly add liquid (tap water and superplasticizer or Ca(NO₃)₂ solution), and mix at low speed with a HOBART planetary mixing machine.
t = 4 min	Stop and scrape the bottom and wall of the container.
t = 4.5 min	Mix at fast speed.
t = 7 min	Stop and fresh cementitious material or acceleration slurry is ready.
Final mixture	
Time	Procedures
t = 0 min	Mix cementitious material or acceleration slurry at low speed with a HOBART planetary mixing machine.
t = 0.5 min	Stop and the final mixture is ready.

inner wall of the building material cell and the small cylindrical cup was equipped with steel lamellas to prevent wall slippage during testing. All rheological tests were performed under a constant temperature of 21 ± 1 °C. The rheological test protocols were reported as follows.

(1) Flow curve test

About 370 ml of fresh CM or AS mortar was prepared and filled into the construction cell. The test protocol of flow curve test is demonstrated in Fig. 4 (a). Before the measurement, a pre-shear with 60 rpm of rotational speed and 30 s duration was applied, and then the fresh sample stayed at rest for 1.5 min. At the material age of 10 min, the rotational speed increased linearly from 0 to 60 rpm for 1.5 min. Afterward, the rotational speed decreased in 6 steps from 60 rpm to 10 rpm and it was kept identical at each step for 1 min. The data was collected every 0.3 s. Fig. 4 (b) illustrates an example of shear stress vs. testing time curve obtained from this test. The measured shear stress ramped with increasing rotational speed and showed a relatively constant value in the descending part under the constant rotational speed. At each step (the descending curve), the average value of the final 50 measuring points, which exhibited a relative equilibrium value, was employed as the shear stress at the applied rotational speed. After applying the plug flow correction [36,51,52], the rotational speed can be converted to shear rate. The obtained shear stresses at the various shear rates are plotted in Fig. 4 (c). By using the Bingham model (Eq (1)), dynamic yield stress τ_d and plastic viscosity μ_p can be determined.

$$\tau = \tau_d + \mu_p \dot{\gamma} \tag{1}$$

where τ means the shear stress and $\dot{\gamma}$ is the shear rate.

(2) Small amplitude oscillatory shear test

As a non-destructive, SAOS-time sweep test can monitor the evolution of elasticity and rigidity of fresh cementitious pastes [53,54]. According to Ref. [55], the testing mechanism of SAOS can be explained as follows. A sinusoidal oscillatory strain $\gamma(t)$ is continuously applied to the sample over time (Eq (2)). The measured material response (shear stress $\tau(t)$) was converted to storage modulus G′ and loss modulus G″ by using Eq (3) (4).

$$\gamma(t) = \gamma_0 \sin \omega t \tag{2}$$

$$\tau(t) = G^* \gamma(t) \tag{3}$$

(a)

(b)

(c)
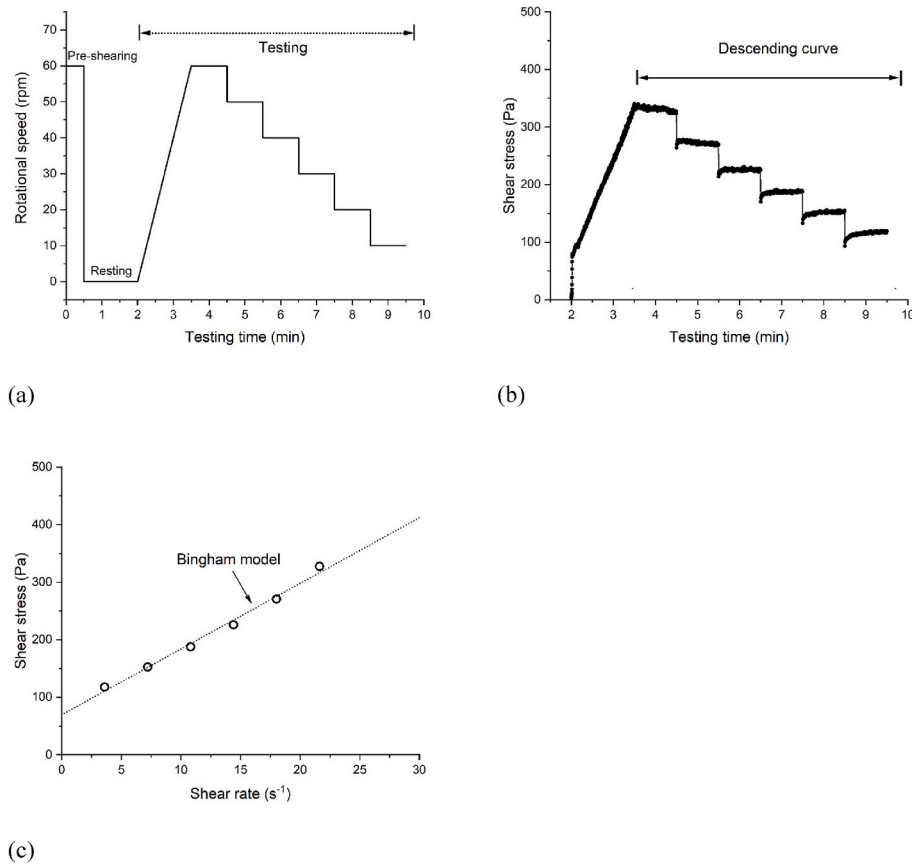
Fig. 4. Flow curve test: (a) Test protocol; (b) An example of shear stress and testing time curve; (c) The average shear stresses at the different shear rates (acquired from the descending curve) were plotted and fitted by the Bingham model.

$$G^* = G' + iG'' \tag{4}$$

where γ_0, t and ω are the maximum strain amplitude, time, and frequency, respectively. G^* means complexed modulus and i represents imaginary unit. G' indicates the in-phase and elastic component, whereas G'' represents the out-of-phase and viscous component (also known as the dissipated energy for each testing cycle). Loss factor, as the ratio between G'' and G', is usually employed to reveal the rigidity of tested material. The higher rigidity, the smaller the loss factor.

For SAOS-time sweep test, the acquired G' remains independent only when the applied strain amplitude is within the linear viscoelasticity regime (LVER). To determine LVER of studied mixtures, a strain sweep (applied strain of 0.001 %–50 % and the frequency of 1 Hz) test was initially conducted at material age of 10 min. After that, a SAOS-time sweep test was immediately executed at 0.005 % strain amplitude (this strain is in LVER of studied materials according to strain sweep test results in Section 3.2.1) and a constant frequency of 1 Hz at the material age of 22 min. This test lasted about 50 min, and the data were recorded every 36 s. About 88 g of fresh paste (final mixture) for each measurement was filled in the small cylinder cup. Note that the pre-shear session (100 rpm of rotational speed and 30 s of duration) and 30 s of resting time were also applied before the start of strain sweep test.

2.3.3. Initial setting time and inline buildability tests

The initial setting time of different final mixtures was measured by an automatic Vicat apparatus. The test was performed in accordance with the specifications of NEN-EN 196–3 [56]. As introduced in Section 2.1, the set-on-demand printing setup was employed to perform the inline buildability test. A hollow cylinder with a 250 mm diameter (the diameter of the printing path) was printed using different mixtures to

assess their buildability performance. A nozzle with a round opening (diameter: 25 mm) was used. The nozzle was moved up to a height of 15 mm during the printing of each layer. Thus, the designed layer thickness was about 15 mm. The pumping rate of 50 rpm was kept identical for CM and AS, and the nozzle moving speed was selected as 60 mm/s, resulting in a 13.1 s time interval between two layers. The abovementioned printing parameters are summarized in Table 3. The maximum layer number before collapsing was the leading indicator for this test.

2.3.4. Characterization of early-age hydration and compressive strength

Early-age hydration and compressive strength of final mixtures (see Table 4) were characterized in this study to determine the effect of Ca $(NO_3)_2$ solution. An eight-channel TAM Air isothermal calorimeter was used to measure the hydration heat released during the first 7 days. The pre-mixed liquid consisting of water, SP and Ca$(NO_3)_2$ solution (except the reference mixture) was mixed with the pre-weighed binding materials using a small mixing machine for about 3 min. Then, together with

Table 3
Dimension of the printed object and printing parameters for the buildability assessment.

Printed object	
Designed diameter (printing path) of cylindrical hollow	250 mm
Designed layer number of cylindrical hollow	16

Printing parameters	
Material flow rate	1.32 L/min
Nozzle moving speed	60 mm/s
Nozzle orifice size (diameter)	25 mm
Nozzle standoff distance	15 mm
Time interval between layers	13.08 s

Table 4

The composition of final mixtures prepared by mixing cementitious material and acceleration slurry.

Final mixture	Cementitious material + acceleration slurry	Volume ratio of two mixtures	Portland cement [kg/m³]	Limestone powder [kg/m³]	Calcined clay [kg/m³]	Water [kg/m³]	Aggregate [kg/m³]	Superplasticizer [kg/m³]	$Ca(NO_3)_2$ [kg/m³]
F-0	CM-0.6 + AS-0	1:1	275	575	150	300	1000	3	0
F-1	CM-0.6 + AS-7	1:1	275	575	150	280	1000	3	35
F-2	CM-0.6 + AS-14	1:1	275	575	150	260	1000	3	70

the reference vessel (filled with fine quartz sand), the sample vessel containing 6 g of fresh paste was placed in the machine at 20 °C. These paste samples were also employed for thermogravimetric analysis (TGA) and qualitative X-ray diffraction (XRD) analysis. Until the time to stop hydration, i.e., 1 h, 4 h, and 7 days, paste samples were stored in sealed cylindrical plastic cups at an ambient temperature of 20 ± 2 °C. A three-step procedure (including solvent exchange method with isopropanol) reported by Lothenbach et al. [55] was used to prepare TGA and XRD powder samples. TGA was performed on Netzsch STA 449 F3 Jupiter. About 50 mg of powder sample for each test was filled in an alumina crucible and heated from 40 to 900 °C at a heating rate of 10 °C/min under an argon environment. XRD was employed to characterize the crystalline phases of studied mixtures formed at different ages. XRD patterns were determined using Bruker D8 advance diffractometer, with Cu-Kα source operated at 45 kV and 40 mA. Sample was scanned from 10° to 70° diffraction angle (2θ) with a step size of 0.010° 2θ.

Cubic mortar samples (40 mm) of different final mixtures were cast and tested at the material age of 7, 28 and 56 days to investigate the influence of $Ca(NO_3)_2$ solution on compressive strength. The main reason for using cast samples rather than printed samples is to consider the impacts of the printing process on compressive strength. According to earlier studies [57,58], different printing processes can result in varying interlayer bonding strengths, thereby influencing the compressive strength of printed samples. In this context, the main issue we considered was the effect of calcium nitrate dosage. To eliminate the effect of the printing process, cast samples were therefore employed in the current work. All samples were cured in sealed plastic bags at an ambient temperature of 20 ± 2 °C until the time of testing. The compressive strength test was conducted at a loading rate of 2.4 kN/s in accordance with NEN-EN 196–1 [59]. The compressive strength of each mixture at different ages was the average value of three repeat tests.

3. Results and discussions

3.1. Flow behavior

3.1.1. Flowability

Fig. 5 (a) shows slump flow test results of CM with different dosages

of SP within the first 1 h. The increase in SP dosage significantly increased flowability of CM. From 10 min to 1 h, the spread diameter of all CM mixtures decreased by nearly 40 mm. The fluidity loss could be attributed to the water evaporation, flocculation of cementitious particles, and/or the interaction between PCE-based SP and hydrated aluminate phases, ettringite and calcined clay due to the chemical/physical adsorption [60,61]. As reported by Refs. [62,63], the Ca^{2+} in the pore solution can be adsorbed by calcined clay, making the negative zeta potential on the surface of calcined clay almost neutral or even positive. The adsorbed Ca^{2+} layer on the surface of calcined clay promotes PCE adsorption. This effect largely weakens the dispersion of PCE, lowering slump flow retention of mixtures containing calcined clay. The spread diameters of AS with different dosages of $Ca(NO_3)_2$ solution are reported in Fig. 5 (b). Increasing the addition of $Ca(NO_3)_2$ solution increased the ion concentration and viscosity of mixing water, resulting in the flowability reduction of AS. Furthermore, the spread diameter of AS mixtures decreased with increasing resting time, which was caused by free water loss due to the absorption of fine sand and evaporation. Within the first hour, the spread diameter of all AS mixtures was in the range of 180–220 mm. Mixture CM-0.6 exhibited a similar range of values compared to AS mixtures. According to earlier studies [33,38], relatively homogenous final mixture may be obtained using two components (CM and AS) with similar rheological behaviors. Therefore, mixture CM-0.6 and AS mixtures were selected for further study.

3.1.2. Flow curve

Flow curve test results of mixtures CM-0.6, AS-0, AS-7, and AS-14 are reported in Fig. 6. Fig. 6 (a) illustrates the linear relationship (the Bingham model) between shear rates and shear stresses for studied mixtures. The dynamic yield stress and plastic viscosity were computed and summarized in Fig. 6 (b) (c). For AS mixtures, the increase in the dosage of $Ca(NO_3)_2$ solution increased dynamic yield stress, which is consistent with the flowability results in Section 3.1.1. Mixture CM-0.6 showed slightly higher dynamic yield stress than mixture AS-7 but lower than mixture AS-14. All mixtures displayed similar plastic viscosities considering the standard deviations. Both the dynamic yield stress and plastic viscosity of developed mixtures are much smaller than that of typical 3D printable mixtures (dynamic yield stress>600 Pa [51]; plastic

(a)   (b)
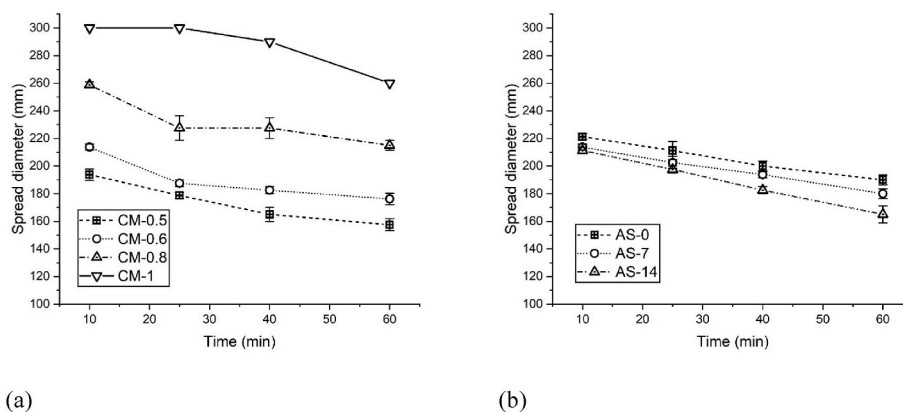
Fig. 5. Flowability test results: (a) Cementitious materials with different superplasticizer dosages – spread diameter at different resting times; (b) Acceleration slurries with different accelerator dosages – spread diameter at different resting times. Error bars mean the standard deviation of repeated test results.
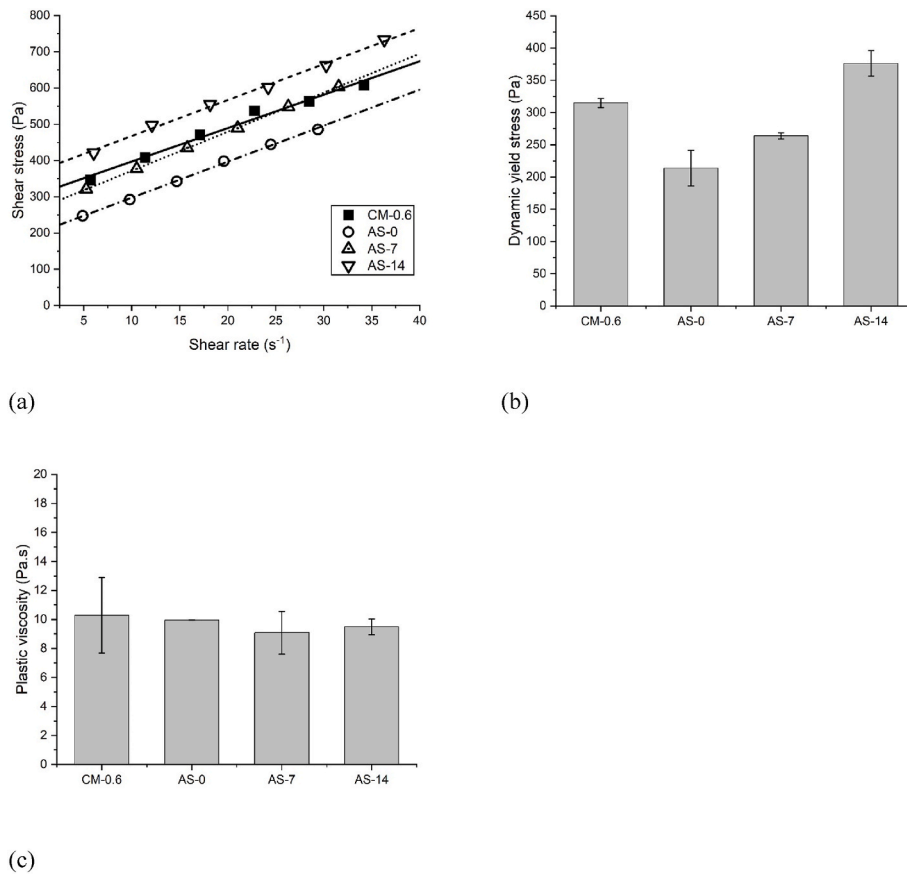
Fig. 6. Flow curve test results: (a) Shear stress as a function of shear rate (fitted by the Bingham model); (b) Dynamic yield stress and (c) plastic viscosity of different mixtures. Error bars mean the standard deviation of repeated test results.

viscosity>15 Pa s [64]), which is beneficial for decreasing the pumping pressure [36].

3.1.3. Pumpability

The inline pumpability test was examined for mixtures CM-0.6 and AS-7. Fig. 7 shows the strong linear correlation between pump and
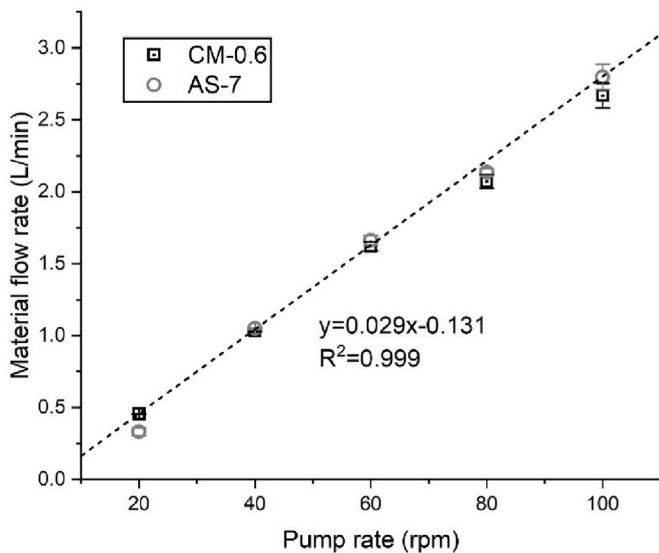
Fig. 7. Pumpability test results (material flow rates at the different pump rates) of mixtures CM-0.6 and AS-7. Error bars mean the standard deviation of repeated test results.

material flow rates (R squared value is higher than 0.99). Both mixtures CM-0.6 and AS-7 can reach a similar flow rate under the same pump rotation speed. Thus, by applying the same rotation speed, the conveyed volume ratio between mixtures CM-0.6 and AS-7 in the inline static mixer can be kept as 1:1. In this study, the final mixture was made by mixing CM and AS at the volume ratio of 1:1, as shown in Table 4. By using this volume ratio, the Portland cement content in the final mixture was about 275 kg/m^3 in the final mixture, remarkably lower than most of the proposed 3D printable cementitious materials according to Ref. [42]. Further reduction of CM would result in a 28-day compressive strength of less than 30 MPa. Besides, the use of the same rotational speed for two pumps allows for easy control over the similar volume of CM and AS. Note that Ca(NO$_3$)$_2$ dosages in final mixtures F-1 and F-2 were 6.36 % and 12.73 % by weight of Portland cement (the dosage was calculated based on the mass of dry calcium nitrate), respectively.

3.2. Stiffness evolution with time and buildability

3.2.1. Structural build-up and initial setting time

Fig. 8 reports initial setting time of final mixtures with different contents of Ca(NO$_3$)$_2$ solution. The initial setting time was expected to be reduced by increasing the Ca(NO$_3$)$_2$ solution dosage. The setting time was nearly an hour shortened by blending AS-7. The initial setting was further accelerated by about 0.5 h by increasing the content of Ca(NO$_3$)$_2$ from 6.36 % to 12.73 %. Due to cleaning and testing constraints in the laboratory, the final mixture of less than 50 min (mixture F-2) was not used for the SAOS-time sweep and inline buildability tests. Note, however, that mixture F-2 is still possible to implement in practice.

Fig. 9 (a) shows the strain sweep test results (material age: 10 min) of mixtures F-0 and F-1. As can be observed, all storage modulus G′ and loss modulus G″ curves exhibited an increase in development with time until
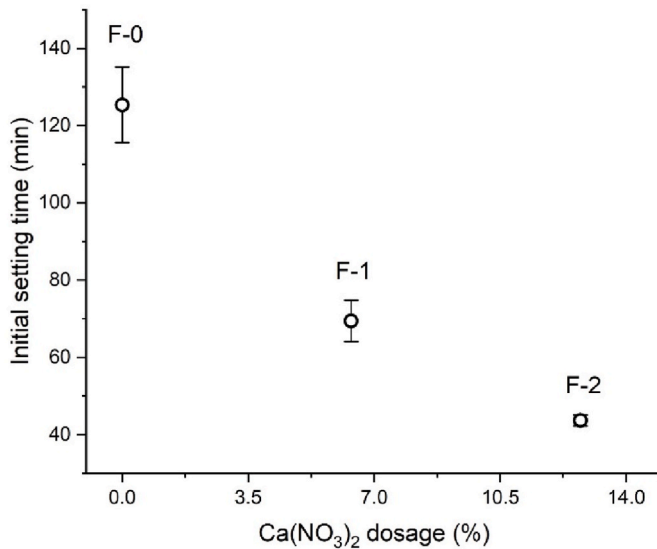
Fig. 8. Initial setting time results of final mixtures with different accelerator dosages. Error bars mean the standard deviation of repeated test results.

they reached a peak value at the applied strain of 0.07 %. After that, these curves decreased with increasing the applied strain. According to earlier studies [65,66], the critical strain can be defined as the applied strain starting to disturb the microstructure of fresh cementitious materials. Thus, in this case, the critical strain of both mixtures was around 0.07 %. This can confirm that the applied strain amplitude of 0.005 % in SAOS-time sweep is appropriate for both mixtures. As mentioned earlier, the magnitude of G′ and G″ is independent within LVED. Therefore, the growth in G′ appeared to be attributed to the (re-)flocculation of cementitious particles at rest [67].

Fig. 9 (b) compares the development of G′ and loss factor G''/G′ with resting time (material age: 22–72 min) of mixtures F-0 and F-1. For both mixtures, G′ evolved slowly, but loss factor increased rapidly within the first 3 min. This means that the increase in G″ was faster than that of G'. The presence of SP in the system seemed to weaken the flocculation and enhance the liquidation/gelation. Afterward, loss factor displayed a steep drop, while G′ showed a near-linear rapid evolution from 3 min to 25–30 min. According to Refs. [66,68,69], this process is dominated by the flocculation of cementitious particles, forming a network of colloidal interactions. After that, the evolution of G′ and loss factor became slower, which may indicate the formation of a percolated rigid network induced by the precipitation and nucleation of hydration products (i.e., C–S–H) at the pseudo-contact points between particles. Compared to mixture F-0, mixture F-1 exhibited a much higher G′ after 3 min and a smaller loss factor after 7 min, which correlates with higher elasticity
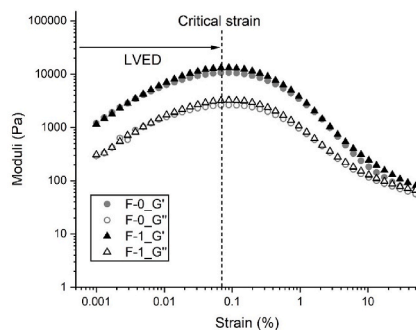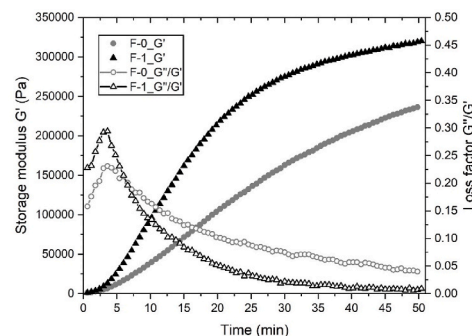
and rigidity development. This promotion of structural build-up appeared to be attributed to the addition of Ca(NO₃)₂ solution.

3.2.2. Buildability assessment

The buildability test results are reported in Fig. 10. As can be observed, mixture F-1 can stack at least 16 layers (height: 240 mm) without any clear layer deformation and showed a much better buildability than mixture F-0. Note that the buildability limit of mixture F-1 cannot be reached with the current printing setup owing to its insufficient vertical range of motion. However, the current test is sufficient to indicate the enhancement of buildability by adding Ca(NO₃)₂ solution. For mixture F-0, there was almost no plastic deformation of the printed hollow cylinder until the deposition of the 11th layer. The bottom layer was severely squeezed, resulting in improper layer deposition. Consequently, the buckling collapse of the printed structure occurred at the lay-up of the 16th layer, which was initiated by this local/global instability.

3.3. Early-age hydration and compressive strength

3.3.1. Hydration kinetics

Fig. 11 compares the heat flow (24 h and 126 h) and cumulative heat (7 days) normalized by the sample mass of paste mixtures containing 0 %, 6.36 %, and 12.73 % of Ca(NO₃)₂. As shown in Fig. 11 (a), mixtures F-1 and F-2 showed an earlier onset of acceleration stage (appeared around 1 h of hydration), much higher intensity of flow rate during the dormant period, earlier appearance time (about 4 h) and higher value of the main hydration peak, compared to the reference mixture (F-0). These phenomena appeared to be governed by the stimulation of Ca(NO₃)₂ on C_3S and C_3A reactions. The high concentration of Ca^{2+} in the pore solution can promote C–S–H nucleation [70]. Also, a fast supersaturation of the pore solution was easily achieved by adding Ca(NO₃)₂, resulting in early portlandite precipitation and accelerated C_3S hydration [71]. The intensity of the main hydration was enhanced by the increase in Ca^{2+} concentration.

However, compared to mixture F-2, mixture F-1 had a much higher heat flow during the dormant period. This effect could be attributed to the C_3A hydration induced by the initial precipitation of gypsum. Dorn et al. [41] pointed out that the presence of Ca(NO₃)₂ may cause the rapid precipitation of gypsum at the beginning of hydration but then promote gypsum dissolution at a higher rate than the mixture without Ca(NO₃)₂. Thus, the temporary gypsum depletion appears at the dormant period in the case of mixture F-1, leading to a relatively high heat flow. In contrast, this precipitation may happen earlier in the case of mixture F-2. Increasing the Ca(NO₃)₂ solution dosage from 6.36 % to 12.73 % may also slightly inhibit the dissolution of reactive aluminate, which needs further confirmation. Additionally, the dissolution rate of gypsum seemed to be enhanced by increasing the content of Ca(NO₃)₂ solution. As a consequence, the formation of ettringite (see Section 3.3.2) at 1 h

(a)   (b)

Fig. 9. SAOS test results: (a) Strain sweep of mixtures F-0 and F-1; (b) Time sweep of mixtures F-0 and F-1.
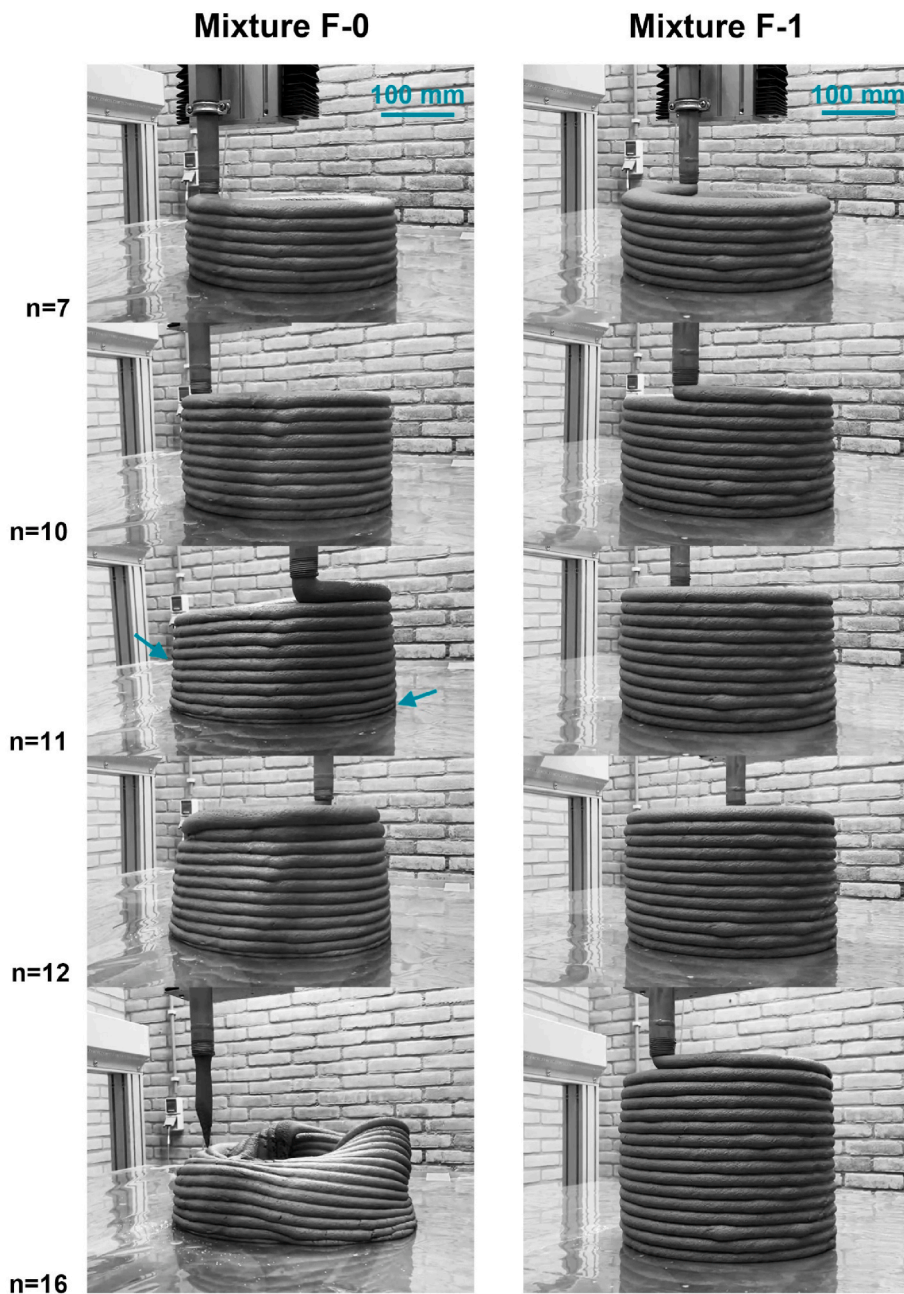
Fig. 10. Buildability test results (hollow cylinder with 250 mm printing path diameter) of mixtures F-0 and F-1. The cyan arrows indicated the onset of plastic deformation. (For interpretation of the references to colour in this figure legend, the reader is referred to the Web version of this article.)

and 4 h appeared to be promoted, which is in line with [41]. For mixture F-0, a sharp and high aluminate peak (9–10 h) occurred immediately after the main hydration peak, owing to the temporary gypsum depletion. As reported by Refs. [72,73], gypsum may be adsorbed on surfaces of C–S–H and calcined clay/metakaolin particles leading to the temporarily unavailable sulfate in the system. Besides, adding $Ca(NO_3)_2$ solution seemed to increase sulfate availability at an early age owing to the formation of NO_3-AFm, alleviating sulfate consumption [41,50].

A small hump was found in studied mixtures after 48 h of hydration, which may be linked to the pozzolanic reaction between calcium hydroxide and calcined clay, corresponding to the formation of hemi-/mono-carboaluminate (CO_3-AFm) [15,74]. The increase in the dosage of $Ca(NO_3)_2$ solution can slightly accelerate the appearance time of this hump. Overall, the 7 day-hydration of calcined clay and limestone-based cementitious material was enhanced by the addition of $Ca(NO_3)_2$

solution. As shown in Fig. 11 (b), mixtures F-1 and F-2 showed much higher cumulative heat than mixture F-0 within the first 7 days. Only a very small increase was achieved by increasing the content of $Ca(NO_3)_2$ solution from 6.36 % to 12.73 %.

3.3.2. TGA and XRD

Fig. 12 (a) (b) (c) illustrate the thermogravimetric (TG) and derivative thermogravimetric (DTG) results of mixtures F-0, F-1, and F-2 at the material age of 1 h, 4 h, and 7 days. As can be observed, a prominent peak at 100–150 °C in DTG curves indicated water loss of C–S–H gel layer and ettringite [75]. After that, a small peak at 150–200 °C, especially for mixtures F-0 and F-1 at 7 days, revealed the decomposition of monocarboaluminate (CO_3-AFm), according to Ref. [76]. For mixtures containing $Ca(NO_3)_2$, a peak was found at 250–300 °C, which may be related to the mass loss of nitrate-containing AFm (NO_3-AFm) [50,77].
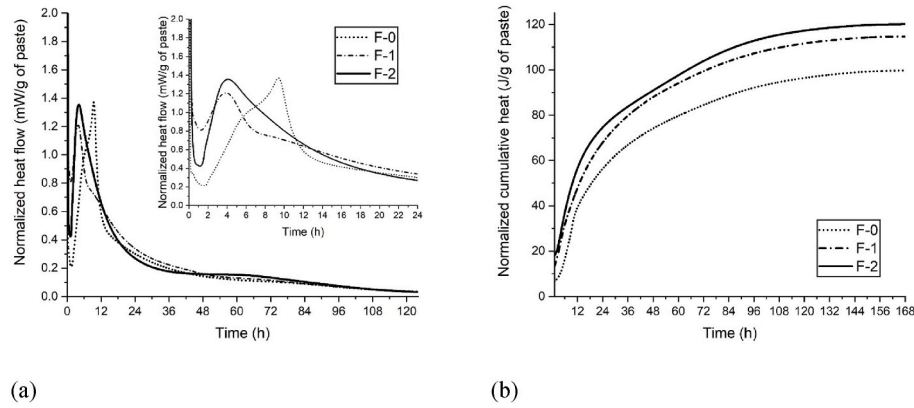
Fig. 11. Isothermal calorimetry test results: (a) Heat flow normalized by paste weight with time (24 h and 126 h); (b) Cumulative heat normalized by paste weight with time (7 days).

This peak intensity appeared to be enhanced by the increased content of $Ca(NO_3)_2$. In contrast, increasing $Ca(NO_3)_2$ dosage reduced the intensity of CO_3-AFm peak. Clearly, NO_3-AFm is more favorable to form compared to the CO_3-AFm in the case of high NO_3^- concentration, which is in good agreement with the findings of [41,50]. The decomposition temperature of calcium hydroxide (portlandite) was in the temperature range of 360–500 °C, and the amount of portlandite can be calculated using Eq (5). Additionally, as reported by Refs. [24,76,78], the chemically bound water content can be quantified by determining the mass loss in the range of 40–600 °C (see Eq (6)).

$$W_{[Ca(OH)_2]} = \frac{M_{360°C} - M_{500°C}}{M_{600°C}} \times \frac{m_{[Ca(OH)_2]}}{m_{[H_2O]}} \times 100(\%) \tag{5}$$

$$W_{[H_2O]} = \frac{M_{40°C} - M_{600°C}}{M_{600°C}} \times 100(\%) \tag{6}$$

here $W_{[H_2O]}$ and $W_{[Ca(OH)_2]}$ mean the mass percentages of chemically bound water and calcium hydroxide in the mixtures. $m_{[Ca(OH)_2]}$, and $m_{[H_2O]}$ are the molar masses of calcium hydroxide (74 g/mol) and water (18 g/mol). $M_{40°C}$, $M_{360°C}$, $M_{500°C}$ and $M_{600°C}$ represent the mass percentages at 40 °C, 360 °C, 500 °C, and 600 °C. Fig. 12 (d) and (e) summarize the chemically bound water and calcium hydroxide contents of studied mixtures. Mixtures with $Ca(NO_3)_2$ showed a higher portlandite content than the reference mixture (F-0) at all tested ages. As mentioned earlier, the Ca^{2+} concentration was significantly increased by adding $Ca(NO_3)_2$, which promoted massive portlandite precipitation. However, this promotion was not found between mixtures F-1 and F-2 within the first 4 h. At 7 days, mixture F-2 displayed a higher portlandite content than mixture F-1, confirming the increased hydration by adding a higher dose of $Ca(NO_3)_2$. As shown in Fig. 12 (e), the addition of Ca $(NO_3)_2$ largely increased the chemically bound water content, especially within the first 4 h. Compared to mixture F-1, mixture F-2 had a higher amount of chemically bound water at all material ages. The increase in chemically bound water content comes not only from C–S–H gel and portlandite, but also from ettringite and AFm phases. The presence of Ca $(NO_3)_2$ can stimulate the formation of ettringite (see Fig. 13) at a very early age (1 h and 4 h) appeared to be the dominant reason for mixture F-2 with the highest chemically bound water content than others. Overall, increasing the dosage of $Ca(NO_3)_2$ improved 7 day-hydration of limestone-calcined clay-based cementitious materials. A strong linear correlation between chemically bound water content and normalized cumulative heat (from isothermal calorimetry) can be achieved.

The XRD patterns of studied mixtures at 1 h, 4 h, and 7 days are reported in Fig. 13. Most of the findings in TGA were confirmed by XRD results. Compared with the reference mixture (F-0), mixtures F-1 and F-2 showed much higher intensity of ettringite at 1 h and 4 h. This is consistent with earlier studies [50,79] which mentioned that nitrate in

the pore solution enhances early-age ettringite formation. In addition, the ettringite precipitated within the first 1 h also boosted the buildability, structural build-up and shortening initial setting time (see Figs. 8–10) for mixtures containing $Ca(NO_3)_2$. CO_3-AFm and/or NO_3-AFm were not observed during the first 4 h but were detected at the material age of 7 days. According to Refs. [46,74], CO_3-AFm was formed by the reaction of calcite, portlandite (CH), metakaolin (A) from calcined clay and/or C_3A as shown in Eq (7) (8).

$$A + 3.5CH + 0.5C\overline{C} + 8.5H \rightarrow C_4A\overline{C}_{0.5}H_{12} \tag{7}$$

$$C_3A + 0.5CH + 0.5C\overline{C} + 11.5H \rightarrow C_4A\overline{C}_{0.5}H_{12} \tag{8}$$
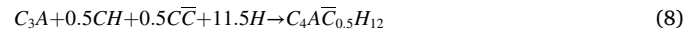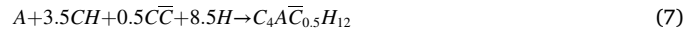
The increase in the dosage of $Ca(NO_3)_2$ can increase the content of NO_3-AFm, which adversely affects the formation of CO_3-AFm. Nitrate appears to show a much stronger AFm binding capacity than CO_3^{2-} and SO_4^{2-} [41,50], which may be due to the very high NO_3^- concentration in the pore solution. Also, the ettringite peak intensity was reduced in mixtures F-1 and F-2, probably due to the formation of NO_3-AFt, as reported by Ref. [80]. However, NO_3-AFt was not detected in the current XRD patterns, which still needs to be confirmed by further study.

3.3.3. Compressive strength

The compressive strength of studied mixtures at 7, 28 and 56 days are presented in Fig. 14. The increase in the dosage of $Ca(NO_3)_2$ slightly improved the compressive strength at 7 days but significantly enhanced that at 28 days. This enhancement was also reported in earlier studies [41,81]. The rise in compressive strength can be attributed to the enhanced degree of hydration and densification of microstructure. According to Dorn et al. [41], adding $Ca(NO_3)_2$ can increase the total phase volume of the hydrated cementitious material, which may be linked to the formation of NO_3-AFm and increased amount of C–S–H gels. However, at 56 days, all studied mixtures showed similar compressive strengths. The increase in compressive strength from 28 days to 56 days decreased with increasing the dosage of $Ca(NO_3)_2$. The compressive strength of mixture F-2 at 28 days and 56 days was almost the same taking into account the standard deviation. This indicated that $Ca(NO_3)_2$ only enhances the compressive strength by accelerating early-age hydration (within 28 days).

Please note that the compressive strength in this context is also influenced by the homogeneity of the printed material. The homogeneity of the printed material in the 2 K system should be considered from two perspectives: the mixing homogeneity of CM and AS in each filament, and the interface between two filaments or layers. The former relies on the number of mixing units in the static mixer. Increasing the number of mixing units can significantly improve the mixing grade of CM and AS [33]. Concerning interlayer bonding, it is adversely affected by the enhanced thixotropy of the printable material caused by the
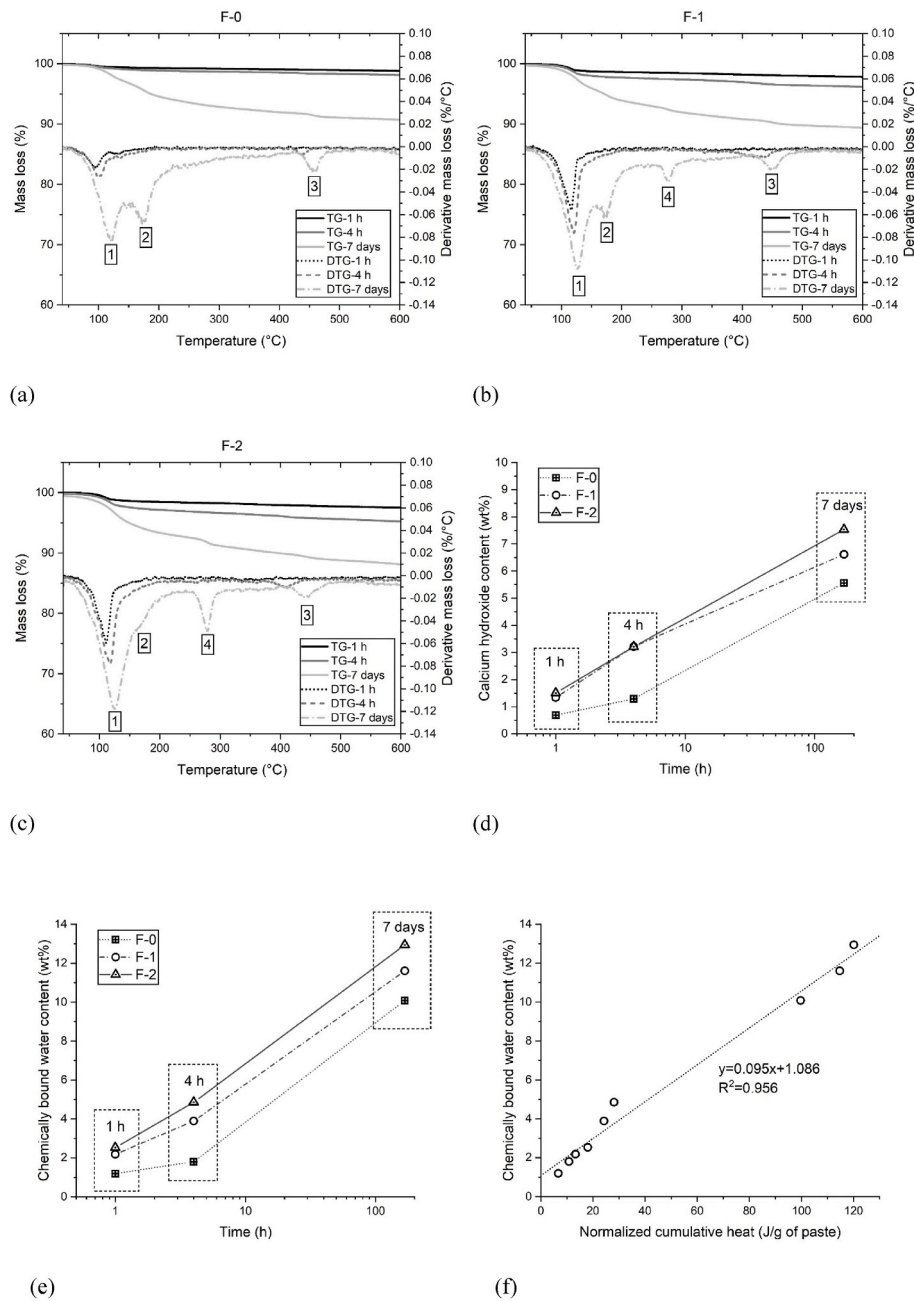
Fig. 12. TGA of different final mixtures at 1 h, 4 h, and 7 days: (a) TG and DTG curves of mixture F-0; (b) TG and DTG curves of mixture F-1; (c) TG and DTG curves of mixture F-2.1- ettringite and C–S–H, 2- CO_3-AFm, 3- calcium hydroxide (portlandite), 4- NO_3-AFm. (d) Calcium hydroxide content normalized by the dry sample mass at 600 °C; (e) The content of chemically bound water normalized by the dry sample mass at 600 °C; (f) The correlation between normalized cumulative heat and chemically bound water content.

addition of accelerators in the case of 2 K printing. Additionally, inter-layer bonding is influenced by printing parameters such as time interval, temperature, and relative humidity (RH) in the printing environment [57,58,82]. Further investigation into the homogeneity of the developed materials in the 2 K system will be conducted in the future.

4. Conclusions

The main goal of this article was to propose an approach to develop limestone-calcined clay-based cementitious materials activated with Ca (NO$_3$)$_2$ solution based on an inline static mixer-based 3DCP setup. Two kinds of pumpable mixtures, i.e., cementitious materials (CM) and limestone-based acceleration slurries (AS), were formulated using slump

flow, flow curve, and pumpability tests. After (inline) mixing CM and AS at a volumetric ratio of 1:1, the buildability performance, initial setting time, elasticity, and rigidity evolution of final mixtures were assessed. In addition, the effect of different Ca(NO$_3$)$_2$ dosages on early-age hydration was investigated by a series of material characterization methods. The main findings were summarized as follows.

- For AS, increasing the dosage of Ca(NO$_3$)$_2$ leads to a reduction of flowability, and growth of dynamic yield stress due to the increased ion concentration and viscosity of the pore solution.
- The final printable mixture with a PC content of only about 275 kg/m^3 can be successfully achieved by mixing CM and AS (7 % of Ca(NO$_3$)$_2$ solution) at the volume ratio of 1:1. The designed mixture
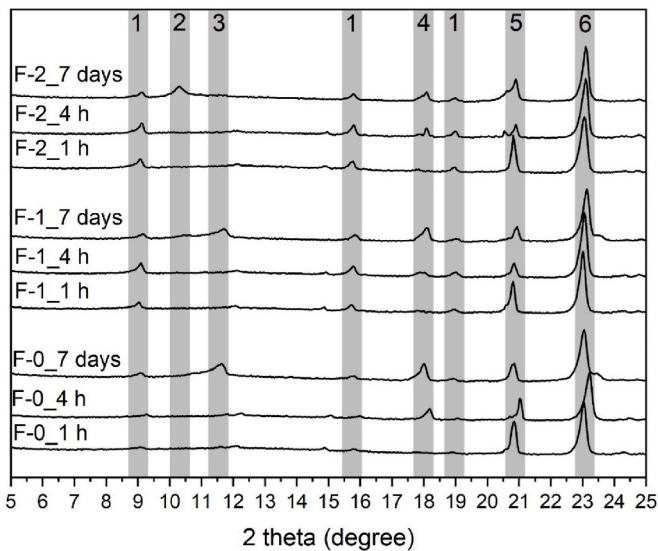
Fig. 13. XRD results of different final mixtures at 1 h, 4 h, and 7 days. 1-ettringite, 2- NO_3-AFm, 3- CO_3-AFm, 4- calcium hydroxide (portlandite), 5-quartz, 6- calcite.
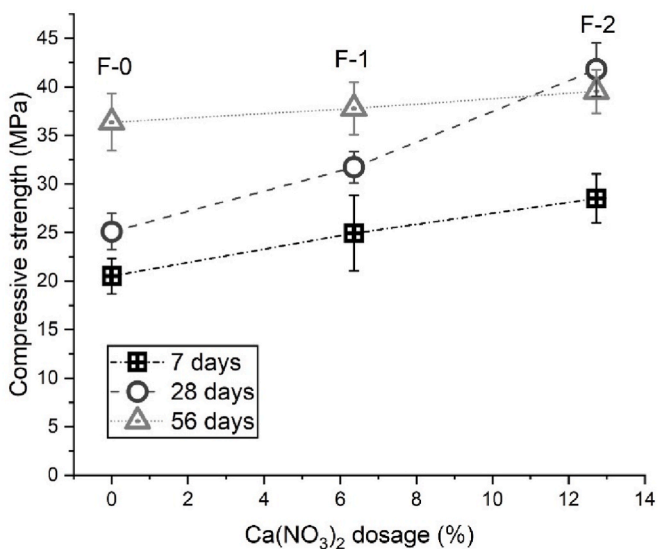
Fig. 14. Compressive strength of different studied mixtures at 7, 28 and 56 days. Error bars mean the standard deviation of repeated test results.

exhibits the required buildability performance as well as a 28-day compressive strength of more than 30 MPa.

- For the final mixtures (F-0 and F-1), the addition of $Ca(NO_3)_2$ results in a reduction of initial setting time, improved buildability performance, and enhanced structural build-up (material age: 22–72 min). The reduced initial setting time and boosted elasticity (G′ growth) and rigidity (decrease in loss factor) evolution can be attributed to the formation of ettringite and promoted *C*–S–H nucleation due to the high concentration of Ca^{2+} in the pore solution.
- Increasing the dosage of $Ca(NO_3)_2$ in the final mixtures (F-0, F-1 and F-2) accelerated early-age hydration of LC3 paste within the first 7 days, i.e., the accelerated onset of acceleration stage and main hydration, the increased amount of cumulative heat, portlandite and chemically bound water. Compressive strength at 7 and 28 days was also enhanced by the use of $Ca(NO_3)_2$. The improvement of

compressive strength seemed to be related to the formation of NO_3-AFm and the increase in the amount of *C*–S–H gels.

CRediT authorship contribution statement

Yu Chen: Conceptualization, Data curation, Formal analysis, Investigation, Methodology, Supervision, Visualization, Writing – original draft, Writing – review & editing. **Hossein Rahmani:** Investigation. **Erik Schlangen:** Supervision, Writing – review & editing. **Oğuzhan Çopuroğlu:** Funding acquisition, Resources, Supervision, Writing – review & editing.

Declaration of competing interest

On behalf of all the authors, we declare that all authors have no conflict of interest regarding the content of the research as written in the submitted article.

Data availability

Data will be made available on request.

Acknowledgments

The authors acknowledge Mr. John van den Berg for his technical support in the experimental tests. Mr. Ruud Hendrikx at the Department of Materials Science and Engineering of TU Delft is acknowledged for the X-ray analysis.

References

[1] R.J. Flatt, T. Wangler, On sustainability and digital fabrication with concrete, Cement Concr. Res. 158 (2022), 106837, https://doi.org/10.1016/j.cemconres.2022.106837.
[2] T. Wangler, R. Pileggi, S. Gürel, R.J. Flatt, A chemical process engineering look at digital concrete processes: critical step design, inline mixing, and scaleup, Cement Concr. Res. 155 (2022), 106782, https://doi.org/10.1016/j.cemconres.2022.106782.
[3] G. De Schutter, K. Lesage, V. Mechtcherine, V.N. Nerella, G. Habert, I. Agusti-Juan, Vision of 3D printing with concrete — technical, economic and environmental potentials, Cement Concr. Res. 112 (2018) 25–36, https://doi.org/10.1016/j.cemconres.2018.06.001.
[4] F. Bos, R. Wolfs, Z. Ahmed, T. Salet, Additive manufacturing of concrete in construction: potentials and challenges of 3D concrete printing, Virtual Phys. Prototyp. 11 (2016) 209–225, https://doi.org/10.1080/17452759.2016.1209867.
[5] V. Mechtcherine, F.P. Bos, A. Perrot, W.R.L. da Silva, V.N. Nerella, S. Fataei, R.J. M. Wolfs, M. Sonebi, N. Roussel, Extrusion-based additive manufacturing with cement-based materials – production steps, processes, and their underlying physics: a review, Cement Concr. Res. 132 (2020), 106037, https://doi.org/10.1016/j.cemconres.2020.106037.
[6] G. Bai, L. Wang, G. Ma, J. Sanjayan, M. Bai, 3D printing eco-friendly concrete containing under-utilised and waste solids as aggregates, Cem. Concr. Compos. 120 (2021), 104037, https://doi.org/10.1016/j.cemconcomp.2021.104037.
[7] A. Perrot, A. Pierre, V.N. Nerella, R.J.M. Wolfs, E. Keita, S.A.O. Nair, N. Neithalath, N. Roussel, V. Mechtcherine, From analytical methods to numerical simulations: a process engineering toolbox for 3D concrete printing, Cem. Concr. Compos. 122 (2021), 104164, https://doi.org/10.1016/j.cemconcomp.2021.104164.
[8] S.H. Chu, L.G. Li, A.K.H. Kwan, Development of extrudable high strength fiber reinforced concrete incorporating nano calcium carbonate, Addit. Manuf. 37 (2021), 101617, https://doi.org/10.1016/j.addma.2020.101617.
[9] M. Chen, H. Li, L. Yang, S. Wang, P. Zhao, Y. Huang, L. Lu, G. Yue, Q. Li, Rheology and shape stability control of 3D printed calcium sulphoaluminate cement composites containing paper milling sludge, Addit. Manuf. 54 (2022), 102781, https://doi.org/10.1016/j.addma.2022.102781.
[10] L. Wang, Y. Liu, Y. Yang, Y. Li, M. Bai, Bonding performance of 3D printing concrete with self-locking interfaces exposed to compression–shear and compression–splitting stresses, Addit. Manuf. 42 (2021), 101992, https://doi.org/10.1016/j.addma.2021.101992.
[11] Y. Chen, S. Chaves Figueiredo, Z. Li, Z. Chang, K. Jansen, O. Çopuroğlu, E. Schlangen, Improving printability of limestone-calcined clay-based cementitious materials by using viscosity-modifying admixture, Cement Concr. Res. 132 (2020), 106040, https://doi.org/10.1016/j.cemconres.2020.106040.
[12] T.T. Le, S.A. Austin, S. Lim, R.A. Buswell, A.G.F. Gibb, T. Thorpe, Mix design and fresh properties for high-performance printing concrete, Mater. Struct. Constr. 45 (2012) 1221–1232, https://doi.org/10.1617/s11527-012-9828-z.

[13] T. Wangler, N. Roussel, F.P. Bos, T.A.M. Salet, R.J. Flatt, Digital concrete: a review, Cement Concr. Res. 123 (2019), 105780, https://doi.org/10.1016/j. cemconres.2019.105780.

[14] A. Perrot, D. Rangeard, A. Pierre, Structural built-up of cement-based materials used for 3D-printing extrusion techniques, Mater. Struct. 49 (2016) 1213–1220, https://doi.org/10.1617/s11527-015-0571-0.

[15] Y. Chen, C.R. Rodriguez, Z. Li, B. Chen, O. Çopuroğlu, E. Schlangen, Effect of different grade levels of calcined clays on fresh and hardened properties of ternary-blended cementitious materials for 3D printing, Cem. Concr. Compos. 114 (2020), 103708, https://doi.org/10.1016/j.cemconcomp.2020.103708.

[16] Y. Chen, S. He, Y. Zhang, Z. Wan, O. Çopuroğlu, E. Schlangen, 3D printing of calcined clay-limestone-based cementitious materials, Cement Concr. Res. 149 (2021), 106553, https://doi.org/10.1016/j.cemconres.2021.106553.

[17] B. Panda, J.H. Lim, M.J. Tan, Mechanical properties and deformation behaviour of early age concrete in the context of digital construction, Composites, Part B 165 (2019) 563–571, https://doi.org/10.1016/j.compositesb.2019.02.040.

[18] B. Panda, S. Ruan, C. Unluer, M.J. Tan, Improving the 3D printability of high volume fly ash mixtures via the use of nano attapulgite clay, Composites, Part B 165 (2019) 75–83, https://doi.org/10.1016/j.compositesb.2018.11.109.

[19] Y. Weng, M. Li, M.J. Tan, S. Qian, Design 3D printing cementitious materials via Fuller Thompson theory and Marson-Percy model, Construct. Build. Mater. 163 (2018) 600–610, https://doi.org/10.1016/j.conbuildmat.2017.12.112.

[20] V.N. Nerella, M. Näther, A. Iqbal, M. Butler, V. Mechtcherine, Inline quantification of extrudability of cementitious materials for digital construction, Cem. Concr. Compos. 95 (2019) 260–270, https://doi.org/10.1016/j. cemconcomp.2018.09.015.

[21] A.V. Rahul, M. Santhanam, H. Meena, Z. Ghani, 3D printable concrete: mixture design and test methods, Cem. Concr. Compos. 97 (2019) 13–23, https://doi.org/10.1016/j.cemconcomp.2018.12.014.

[22] B. Lu, H. Li, M. Li, T. Neng, S. Qian, Mechanism and design of fluid catalytic cracking ash-blended cementitious composites for high performance printing, Addit. Manuf. 61 (2023), 103286, https://doi.org/10.1016/j.addma.2022.103286.

[23] J. Liu, S. Li, C. Gunasekara, K. Fox, P. Tran, 3D-printed concrete with recycled glass: effect of glass gradation on flexural strength and microstructure, Construct. Build. Mater. 314 (2022), 125561, https://doi.org/10.1016/j. conbuildmat.2021.125561.

[24] Y. Chen, N. Toosumran, N. Chehab, H. Spanjers, O. Çopuroğlu, Feasibility study of using desalination brine to control the stiffness and early-age hydration of 3D printable cementitious materials, J. Clean. Prod. 378 (2022), 134522, https://doi.org/10.1016/j.jclepro.2022.134522.

[25] L. Reiter, T. Wangler, A. Anton, R.J. Flatt, Setting on demand for digital concrete – principles, measurements, chemistry, validation, Cement Concr. Res. 132 (2020), 106047, https://doi.org/10.1016/j.cemconres.2020.106047.

[26] A. Anton, L. Reiter, T. Wangler, V. Frangez, R.J. Flatt, B. Dillenburger, A 3D concrete printing prefabrication platform for bespoke columns, Autom. ConStruct. 122 (2021), 103467, https://doi.org/10.1016/j.autcon.2020.103467.

[27] C. Gosselin, R. Duballet, P. Roux, N. Gaudillière, J. Dirrenberger, P. Morel, Large-scale 3D printing of ultra-high performance concrete - a new processing route for architects and builders, Mater. Des. 100 (2016) 102–109, https://doi.org/10.1016/j.matdes.2016.03.097.

[28] S. Muthukrishnan, S. Ramakrishnan, J. Sanjayan, Effect of microwave heating on interlayer bonding and buildability of geopolymer 3D concrete printing, Construct. Build. Mater. 265 (2020), 120786, https://doi.org/10.1016/j. conbuildmat.2020.120786.

[29] S. Ramakrishnan, S. Kanagasuntharam, J. Sanjayan, In-line activation of cementitious materials for 3D concrete printing, Cem. Concr. Compos. 131 (2022), 104598, https://doi.org/10.1016/j.cemconcomp.2022.104598.

[30] L. Shao, P. Feng, W. Zuo, H. Wang, Z. Geng, Q. Liu, C. Miao, Z. Liu, A novel method for improving the printability of cement-based materials: controlling the releasing of capsules containing chemical admixtures, Cem. Concr. Compos. 128 (2022), 104456, https://doi.org/10.1016/j.cemconcomp.2022.104456.

[31] V. Vaitkevičius, E. Šerelis, V. Kerševičius, Effect of ultra-sonic activation on early hydration process in 3D concrete printing technology, Construct. Build. Mater. 169 (2018) 354–363, https://doi.org/10.1016/j.conbuildmat.2018.03.007.

[32] G. De Schutter, K. Lesage, V. Mechtcherine, V.N. Nerella, G. Habert, I. Agusti-Juan, Vision of 3D printing with concrete — technical, economic and environmental potentials, Cement Concr. Res. 112 (2018) 25–36, https://doi.org/10.1016/j. cemconres.2018.06.001.

[33] Y. Tao, A.V. Rahul, K. Lesage, Y. Yuan, K. Van Tittelboom, G. De Schutter, Stiffening control of cement-based materials using accelerators in inline mixing processes: possibilities and challenges, Cem. Concr. Compos. 119 (2021), 103972, https://doi.org/10.1016/j.cemconcomp.2021.103972.

[34] A. Das, L. Reiter, S. Mantellato, R.J. Flatt, Early-age rheology and hydration control of ternary binders for 3D printing applications, Cement Concr. Res. 162 (2022), 107004, https://doi.org/10.1016/j.cemconres.2022.107004.

[35] F. Boscaro, E. Quadranti, T. Wangler, S. Mantellato, L. Reiter, R.J. Flatt, Eco-Friendly, set-on-demand digital concrete, 3D print, Addit. Manuf. (2021), https://doi.org/10.1089/3dp.2020.0350.

[36] Y. Tao, M.K. Mohan, A.V. Rahul, Y. Yuan, G. De Schutter, K. Van Tittelboom, Stiffening controllable concrete modified with redispersible polymer powder for twin-pipe printing, Cement Concr. Res. 161 (2022), 106953, https://doi.org/10.1016/j.cemconres.2022.106953.

[37] Y. Tao, A.V. Rahul, K. Lesage, K. Van Tittelboom, Y. Yuan, G. De Schutter, Mechanical and microstructural properties of 3D printable concrete in the context of the twin-pipe pumping strategy, Cem. Concr. Compos. 125 (2021), 104324, https://doi.org/10.1016/j.cemconcomp.2021.104324.

[38] M.K. Mohan, A.V. Rahul, Y. Tao, G. De Schutter, K. Van Tittelboom, Hydration re-initiation of borated CSA systems with a two-stage mixing process: an application in extrusion-based concrete 3D printing, Cement Concr. Res. 159 (2022), 106870, https://doi.org/10.1016/j.cemconres.2022.106870.

[39] D. Marchon, S. Kawashima, H. Bessaies-Bey, S. Mantellato, S. Ng, Hydration and rheology control of concrete for digital fabrication: potential admixtures and cement chemistry, Cement Concr. Res. 112 (2018) 96–110, https://doi.org/10.1016/j.cemconres.2018.05.014.

[40] L. Steger, S. Blotevogel, L. Frouin, C. Patapy, M. Cyr, Experimental evidence for the acceleration of slag hydration in blended cements by the addition of CaCl2, Cem, Concr. Res. 149 (2021) 2–10, https://doi.org/10.1016/j.cemconres.2021.106558.

[41] T. Dorn, T. Hirsch, D. Stephan, Working mechanism of calcium nitrate as an accelerator for Portland cement hydration, J. Am. Ceram. Soc. (2022) 1–15, https://doi.org/10.1111/jace.18782.

[42] Y. Chen, S. He, Y. Gan, O. Çopuroğlu, F. Veer, E. Schlangen, A review of printing strategies, sustainable cementitious materials and characterization methods in the context of extrusion-based 3D concrete printing, J. Build. Eng. 45 (2022), 103599, https://doi.org/10.1016/j.jobe.2021.103599.

[43] Y. Chen, F. Veer, O. Copuroglu, A critical review of 3D concrete printing as a low CO2 concrete approach, Heron 62 (2017) 167.

[44] S. Bhattacherjee, A.S. Basavaraj, A.V. Rahul, M. Santhanam, R. Gettu, B. Panda, E. Schlangen, Y. Chen, O. Copuroglu, G. Ma, L. Wang, M.A. Basit Beigh, V. Mechtcherine, Sustainable materials for 3D concrete printing, Cem. Concr. Compos. 122 (2021), 104156, https://doi.org/10.1016/j. cemconcomp.2021.104156.

[45] K. Scrivener, F. Martirena, S. Bishnoi, S. Maity, Calcined clay limestone cements (LC3), Cement Concr. Res. 114 (2018) 49–56, https://doi.org/10.1016/j. cemconres.2017.08.017.

[46] M. Antoni, J. Rossen, F. Martirena, K. Scrivener, Cement substitution by a combination of metakaolin and limestone, Cement Concr. Res. 42 (2012) 1579–1589, https://doi.org/10.1016/j.cemconres.2012.09.006.

[47] W. Long, C. Lin, J. Tao, T. Ye, Y. Fang, Printability and particle packing of 3D-printable limestone calcined clay cement composites, Construct. Build. Mater. 282 (2021), 122647, https://doi.org/10.1016/j.conbuildmat.2021.122647.

[48] B. Shantanu, J. Smrati, S. Manu, Criticality of binder-aggregate interaction for buildability of 3D printed concrete containing limestone calcined clay, Cem. Concr. Compos. 136 (2023), 104853, https://doi.org/10.1016/j. cemconcomp.2022.104853.

[49] J. Skibsted, R. Snellings, Reactivity of supplementary cementitious materials (SCMs) in cement blends, Cement Concr. Res. 124 (2019), https://doi.org/10.1016/j.cemconres.2019.105799.

[50] M. Balonis, M. Mędala, F.P. Glasser, Influence of calcium nitrate and nitrite on the constitution of AFm and AFt cement hydrates, Adv. Cement Res. 23 (2011) 129–143, https://doi.org/10.1680/adcr.10.00002.

[51] M.K. Mohan, A.V. Rahul, K. Van Tittelboom, G. De Schutter, Rheological and pumping behaviour of 3D printable cementitious materials with varying aggregate content, Cement Concr. Res. 139 (2021), 106258, https://doi.org/10.1016/j. cemconres.2020.106258.

[52] P.R. Chhabra, J.F. Richardson, Non-Newtonian Flow and Applied Rheology: Engineering Applications, Cambridge University Press, Cambridge, 2008, https://doi.org/10.1017/CBO9781107415324.004.

[53] Q. Yuan, X. Lu, K.H. Khayat, D. Feys, C. Shi, Small amplitude oscillatory shear technique to evaluate structural build-up of cement paste, Mater. Struct. Constr. 50 (2017) 1–12, https://doi.org/10.1617/s11527-016-0978-2.

[54] A.M. Mostafa, A. Yahia, Physico-chemical kinetics of structural build-up of neat cement-based suspensions, Cement Concr. Res. 97 (2017) 11–27, https://doi.org/10.1016/j.cemconres.2017.03.003.

[55] M.A. Schultz, L.J. Struble, Use of oscillatory shear to study flow behavior of fresh cement paste, Cement Concr. Res. 23 (1993) 273–282, https://doi.org/10.1016/0008-8846(93)90092-N.

[56] NEN-EN 196-3, Methods of Testing Cement. Determination of Setting Times and Soundness, NEN, 2016, p. 18. https://shop.bsigroup.com.

[57] Y. Chen, K. Jansen, H. Zhang, C. Romero Rodriguez, Y. Gan, O. Çopuroğlu, E. Schlangen, Effect of printing parameters on interlayer bond strength of 3D printed limestone-calcined clay-based cementitious materials: an experimental and numerical study, Construct. Build. Mater. 262 (2020), 120094, https://doi.org/10.1016/j.conbuildmat.2020.120094.

[58] R.J.M. Wolfs, F.P. Bos, T.A.M. Salet, Hardened properties of 3D printed concrete: the influence of process parameters on interlayer adhesion, Cement Concr. Res. 119 (2019) 132–140, https://doi.org/10.1016/j.cemconres.2019.02.017.

[59] NEN-EN 196-1, Methods of Testing Cement - Part 1: Determination of Strength, 2016.

[60] S. Bhattacherjee, S. Jain, M. Santhanam, A method to increase the workability retention of concrete with limestone calcined clay based cementitious system using a dispersing agent containing sodium hexametaphosphate, Cem. Concr. Compos. 132 (2022), 104624, https://doi.org/10.1016/j.cemconcomp.2022.104624.

[61] S. Mantellato, M. Palacios, R.J. Flatt, Relating early hydration, specific surface and flow loss of cement pastes, Mater. Struct. Constr. 52 (2019) 1–17, https://doi.org/10.1617/s11527-018-1304-y.

[62] R. Li, L. Lei, T. Sui, J. Plank, Effectiveness of PCE superplasticizers in calcined clay blended cements, Cement Concr. Res. 141 (2021), 106334, https://doi.org/10.1016/j.cemconres.2020.106334.

[63] R. Sposito, M. Maier, N. Beuntner, K. Thienel, Physical and mineralogical properties of calcined common clays as SCM and their impact on flow resistance and demand for superplasticizer, Cement Concr. Res. 154 (2022), 106743, https://doi.org/10.1016/j.cemconres.2022.106743.

[64] M.K. Mohan, A.V. Rahul, K. Van Tittelboom, G. De Schutter, Extrusion-based concrete 3D printing from a material perspective: a state-of-the-art review, Cem. Concr. Compos. 115 (2020), 103855, https://doi.org/10.1016/j.cemconcomp.2020.103855.

[65] M.F. Alnahhal, T. Kim, A. Hajimohammadi, Distinctive rheological and temporal viscoelastic behaviour of alkali-activated fly ash/slag pastes: a comparative study with cement paste, Cement Concr. Res. 144 (2021), 106441, https://doi.org/10.1016/j.cemconres.2021.106441.

[66] A.M. Mostafa, A. Yahia, New approach to assess build-up of cement-based suspensions, Cement Concr. Res. 85 (2016) 174–182, https://doi.org/10.1016/j.cemconres.2016.03.005.

[67] T. Liberto, M. Bellotto, A. Robisson, Small oscillatory rheology and cementitious particle interactions, Cement Concr. Res. 157 (2022), 106790, https://doi.org/10.1016/j.cemconres.2022.106790.

[68] N. Roussel, G. Ovarlez, S. Garrault, C. Brumaud, The origins of thixotropy of fresh cement pastes, Cement Concr. Res. 42 (2012) 148–157, https://doi.org/10.1016/j.cemconres.2011.09.004.

[69] H.A. Barnes, Thixotropy—a review, J. Nonnewton. Fluid Mech. 70 (1997) 1–33, https://doi.org/10.1016/S0377-0257(97)00004-9.

[70] L. Nicoleau, Accelerated growth of calcium silicate hydrates: experiments and simulations, Cement Concr. Res. 41 (2011) 1339–1348, https://doi.org/10.1016/j.cemconres.2011.04.012.

[71] P. Bost, M. Regnier, M. Horgnies, Comparison of the accelerating effect of various additions on the early hydration of Portland cement, Construct. Build. Mater. 113 (2016) 290–296, https://doi.org/10.1016/j.conbuildmat.2016.03.052.

[72] F. Zunino, K. Scrivener, The influence of the filler effect on the sulfate requirement of blended cements, Cement Concr. Res. 126 (2019), 105918, https://doi.org/10.1016/j.cemconres.2019.105918.

[73] F. Zunino, K. Scrivener, Insights on the role of alumina content and the filler effect on the sulfate requirement of PC and blended cements, Cement Concr. Res. 160 (2022), 106929, https://doi.org/10.1016/j.cemconres.2022.106929.

[74] F. Zunino, K. Scrivener, The reaction between metakaolin and limestone and its effect in porosity refinement and mechanical properties, Cem, Concr. Res. 140 (2021), 106307, https://doi.org/10.1016/j.cemconres.2020.106307.

[75] K. De Weerdt, M. Ben Haha, G. Le Saout, K.O. Kjellsen, H. Justnes, B. Lothenbach, Hydration mechanisms of ternary Portland cements containing limestone powder and fly ash, Cement Concr. Res. 41 (2011) 279–291, https://doi.org/10.1016/j.cemconres.2010.11.014.

[76] B. Lothenbach, P. Durdzinski, K. De Weerdt, Thermogravimetric analysis, in: K. Scrivener, R. Snellings, B. Lothenbach (Eds.), A Pract. Guid. To Microstruct. Anal. Cem. Mater., CRC press, 2016, pp. 177–212.

[77] A. Yoneyama, H. Choi, M. Inoue, J. Kim, M. Lim, Y. Sudoh, Effect of a nitrite/nitrate-based accelerator on the strength development and hydrate formation in cold-weather cementitious materials, Materials 14 (2021) 1–14, https://doi.org/10.3390/ma14041006.

[78] R. Roychand, S. De Silva, D. Law, S. Setunge, High volume fly ash cement composite modified with nano silica, hydrated lime and set accelerator, Mater. Struct. Constr. 49 (2016) 1997–2008, https://doi.org/10.1617/s11527-015-0629-z.

[79] B.E.I. Abdelrazig, D.G. Bonner, D.V. Nowell, J.M. Dransfield, P.J. Egan, The solution chemistry and early hydration of ordinary portland cement pastes with and without admixtures, Thermochim. Acta 340–341 (1999) 417–430, https://doi.org/10.1016/s0040-6031(99)00286-5.

[80] Y. Xu, T. He, X. Ma, The influence of calcium nitrate/sodium nitrate on the hydration process of cement paste mixed with alkali free liquid accelerator, Construct. Build. Mater. 347 (2022), 128555, https://doi.org/10.1016/j.conbuildmat.2022.128555.

[81] S. Aggoun, M. Cheikh-Zouaoui, N. Chikh, R. Duval, Effect of some admixtures on the setting time and strength evolution of cement pastes at early ages, Construct. Build. Mater. 22 (2008) 106–110, https://doi.org/10.1016/j.conbuildmat.2006.05.043.

[82] Y. Chen, Z. Chang, S. He, O. Çopuroğlu, B. Šavija, E. Schlangen, Effect of curing methods during a long time gap between two printing sessions on the interlayer bonding of 3D printed cementitious materials, Construct. Build. Mater. 332 (2022), 127394, https://doi.org/10.1016/j.conbuildmat.2022.127394.